Physica B 699 (2025) 416879

Contents lists available at ScienceDirect

Physica B: Condensed Matter

journal homepage: www.elsevier.com/locate/physb

Tuning the optoelectronic, mechanical, and thermodynamic properties of lead-free Mg_3NF_3 perovskite with tunable strain through DFT study

I.K. Gusral Ghosh Apurba [a], Md. Rasidul Islam [a,*], Md Masud Rana [b], Jehan Y. Al-Humaidi [c], A.M. Quraishi [d], Parvez Ali [e], Md. Shizer Rahman [a,**]

[a] Department of Electrical and Electronic Engineering, Bangamata Sheikh Fojilatunnesa Mujib Science & Technology University, Jamalpur, 2012, Bangladesh
[b] Department of Electrical and Computer Engineering, The University of Texas at Tyler, Tyler, 75799, TX, USA
[c] Department of Chemistry, College of Science, Princess Nourah bint Abdulrahman University, P.O. BOX 84428, Riyadh, 11671, Saudi Arabia
[d] Department of Electrical Engineering, College of Engineering, Qassim University, Buraydah, 51452, Saudi Arabia
[e] .Department of Mechanical Engineering, College of Engineering, Qassim University, Buraydah, 51452, Saudi Arabia

ARTICLE INFO

Keywords:
Perovskite
Spin-orbital coupling effect
First-principles analysis
Optical properties

ABSTRACT

Inorganic halide perovskite solar cells have been an enormous breakthrough in the solar energy industry because of their low production costs, high efficiency, and practicality. Structural, electrical, mechanical, and optical traits of Mg_3NF_3 cubic halide perovskites subjected to strain are investigated in this study using first-principle calculation. As a consequence of strain, the electrical energy band gap widens, forcing more electrons to transition from the valence band (VB) to the conduction band (CB) and the visible to the ultraviolet segments of the spectrum. Based on the electrical band structures, the semiconductor substances Mg_3NF_3 molecules have a direct bandgap of 2.98 eV at the location of Γ(gamma). In consideration of the quantum effect of spin-orbital coupling (SOC), the bandgap of the Mg_3NF_3 perovskite is 3.24 eV, correspondingly. Optical features such as dielectric functions, reflectivity, photon absorptions, and loss functions have all been investigated. Some of the predicted factors include elastic constants, Poisson's ratio, Pugh's ratio, and bulk modulus. Studies of this material's elastic attributes reveal that it is anisotropic, ductile, and mechanically stable. The results reveal that when the compressive strain increases, the dielectric constant maxima of Mg_3NF_3 move towards higher photon energy levels. In contrast, when tensile, they engage in red shifting, a transition to lower photon energy levels. The combined effect of these features makes Mg_3NF_3 perovskites a fantastic option for solar power optimization equipment and gadgets that use semiconductors.

1. Introduction

The remarkable optical absorption capabilities and integration of direct bandgaps in cubic inorganic A_3BX_3 structure perovskites are currently being evaluated, making them an intriguing option for use in solar energy, LED, and semiconductor applications [1–3]. A study carried out by L. Zhang et al. proved that perovskite solar cells composed of nonliving halides might deliver large open-circuit voltages on a regular basis [4]. sThe logical conclusion is that perovskite compounds made of inorganic halides and linked solar cells might be the key to unlocking the limitations of ornanicinorganic lead halide perovskite (OILHP) materials. Solar technology companies have expressed a lot of interest in Sr_3AsI_3, Ca_3PI_3, and Ca_3AsI_3 perovskites, which are recognized as A_3BX_3 structure perovskites, because of their uncommon optical, structural, and electrical features [5–7]. Its bandgap was found in an earlier scientific publication, thus it is considered a novel chemical [5,8–10]. The remarkable optical attributes of this perovskite include a high absorption of light, long carrier diffusion intervals, and efficient charge transfer.

Photovoltaic cells convert light into electricity with minimal energy loss [11]. The development of more appealing perovskite material attributes in the last decade has accelerated this trend. A lot of people are interested in inorganic metallic halide perovskites. Perovskites formed from organic-inorganic lead halide are well-known photovoltaic materials due to their economical manufacturing cost, suitable bandgap and broad light absorption spectrum for use in semiconductor device

* Corresponding author.
** Corresponding author.
E-mail addresses: rasidul@bsfmstu.ac.bd (Md.R. Islam), shizer@bsfmstu.ac.bd (Md.S. Rahman).

https://doi.org/10.1016/j.physb.2024.416879
Received 16 October 2024; Received in revised form 13 December 2024; Accepted 30 December 2024
Available online 1 January 2025

manufacture [12–17]. The astonishing features of organic-inorganic perovskites (OILHP) have recently sparked a great deal of experimental enthusiasm in solar technology [7,18–23]. Low reflectivity, a wide availability, a fair bandgap, an impressive optical absorption ability, and a reasonable production cost are the attracive features for optoelecronic device applications. Making semiconductor devices with the right bandgap allows them to absorb light from a broad spectrum [12–17]. The power conversion efficiency (PCE) rose from 3.8 % to 26.1 % throughout the preceding thirteen years [24–26].

Wonderful for solar applications, strain technology allows for the modification of perovskite materials' atomic framework and physical properties. There is a considerable effect of the element utilized on the framework properties of the material, new studies on strain-induced material traits have revealed [27–32]. $CsPbI_3$ measurement under strain, according to Jing et al.'s study [38], allows one to change the strain insertion from −5% to +5 %, which in turn changes the material's bandgap from 1.03 to 2.14 eV. Preserving a bandgap of 1.2–1.4 eV is one strategy for enhancing $CaAsI_3$'s photovoltaic performances [33–35]. Based on studies by A. K. Hossain et al. [36], the inorganic perovskite cubic $CsSnCl_3$ may undergo a transformation into a metallic material when compressively strained, both electrically and optically.

Incorporating compressive or tensile strain into the $CsGeI_3$ perovskite significantly adjusts its bandgap and dielectric function parameters [37]. In general, the spin-orbit coupling (SOC) phenomenon may be used to modify the electrical characteristics of many materials [38,39]. Light elements show less SOC, whereas heavier atoms show a stronger SOC impact [40]. It is believed that SOC evolved via the relativistic effect, allowing electrons to move about in their orbitals and align their spins [41]. Several favorable features of Ca_3PI_3, Ca_3AsI_3, Mg_3AsX_3, and Ca_3PX_3 which we noticed in earlier research [42–45] make it a material with intriguing potential for use in solar cell technology, where it can compete with other materials used in photovoltaic applications. As far as we are aware, no publications have been released concerning the electrical and optical properties of Mg_3NF_3 with combining the effect of strain and SOC. Evaluation of strain's impact and SOC on inorganic Mg_3NF_3 perovskites is therefore, essential for the advancement of future electrical and optoelectronic devices.

The DFT method is employed to achieve this objective. The study focused on the customization of the bandgap, band structure, electron charge density, and stability in Mg_3NF_3. An exhaustive study of the electrical traits of Mg_3NF_3 is performed as it pertains to the implications of the outer strain on the structural features and energy gap. The investigation also finds the characteristics of Mg_3NF_3's absorption spectra, with a particular focus on the shift of the dielectric's most severe points in the red and blue domains because of variable strain conditions. Thus, this investigation verified the stability of Mg_3NF_3 perovskite, bandgap, optical properties, and investigate its mechanical properties. In a nutshell, the results indicate that Mg_3NF_3 could be customized for use in solar energy and optoelectronics by modifying its photonic properties.

2. Computational details

To accomplish the DFT computations, the simulation tool Quantum Espresso (QE) is used [46]. The Mg_3NF_3 perovskite structures were analyzed using the Perdew-Burke-Ernzerhof (PBE) [47] exchange-correlation function and the FP-DFT with a norm-conserving (NC) pseudopotential [32,48]. A Brillouin zone grid, crystal morphologies, kinetic cut-off energy, and fixed lattice parameters are all part of the input data. The structure has been adjusted with a 440 Rydberg (Ry) charge density cut-off and a 50 Rydberg (Ry) kinetic energy cut-off. An accuracy of less than 0.01 eV/ A° and a convergence threshold of 10^{-6} a. u. were adopted in the calculations of the Self-consistent function (SCF). For ionic minimization in relaxation computations, the force convergence threshold is set to 10^{-4} a.u. A 6 × 6 × 6 Monkhorst-Pack k-grid was employed to estimate the band structure and partial density of states (PDOS) of the Brillion zone. For a more precise estimate of the bandgap of Mg_3NF_3 perovskites, the Hyd-Scusena Ernzerhof (HSE-06) hybrid functional is also used. The spectral features of the perovskite structures have been studied by evaluating their convoluted dielectric functions that depend on photon energy, following the estimation of their dynamical stability. To get an overview of the optical properties, we employed the QE package. Functionals known as generalized gradient approximation (GGA) and local density approximation (LDA) were recruited for the computation of organic halides [49]. It was found in our investigation that when the lattice parameter is simultaneously changed, the degree of biaxial strain (comprising compression and tension) ranges from −3% to +3 %, with increments of 1 %. The strain can easily be identified via formula (1) [31]:

$$\varepsilon = \frac{a_{strained} - a_{relaxed}}{a_{relaxed}} \times 100\% \quad (1)$$

The unstrained lattice constant, $a_{relaxed}$, is assumed in the formula, and its range, expressed in units of 1 %, is −3% to +3 %. Consequently, readings that are negative or positive, respectively, indicate the presence of compressive and tensile stresses. For measuring the optical features, we have preserved a 6 × 6 × 6 Monkhorst-Pack k-mesh design that is gamma-centered. In order to figure out the photon energy (eV) range where its absorption maxima were found, the complex dielectric equation is then explored.

3. Results and discussion

3.1. Structural properties

The Pm3m cubic base embodies the periodic pattern of Mg_3NF_3. In the configuration depicted in Fig. 1(a), the single cell splits into seven components. In this material, the Mg and N atoms reside in a cubic lattice, while the F and face-centered atoms occupy an octahedral geography. Mg_3NF_3 bond distances for Mg-N and Mg-F are looked at 2.1709 A° and 2.1709 A° respectively. N^{3-} is joined to six identical Mg^{2+} atoms to create NMg_6 octahedra that share corners. Without a corner, the octahedra has a shared area. Use the 1a, 3c, and 3d Wyckoff sites to estimate Mg, N, and F, which are fractional coordinates of (0.5,0.5,0), (0.5,0.5,0.5), and (0.5,0,0), respectively. Fig. 1(b) depicts the k-path pertaining to the first Brillouin zone. Prior to distinguishing the various properties of Mg_3NF_3 perovskite, it is important to comprehend its structural characteristics. Table 1 displays the findings of the PBE assessment of the structural components pertaining to the lattice constant (A°). When taking the lattice parameter into account and assessing the total energy, the lattice constant of Mg_3NF_3 with the best dependability obtained.

To get the ideal lattice constant for the Mg_3NF_3 material, a projection of the total energy is obtained using an independent variable called the lattice parameter. As displayed in Fig. 2(a), a change in the lattice constant might have been the cause of the total energy. The results are reasonably consistent with the least total energy of the relaxed Mg_3NF_3 structure, which is 4.34 A°. The parameters that decide the optimal structure are the lattice constant, the kinetic cut-off energy, and the amount of k-point items in the circular loop in the Brillouin zone (BZ). Furthermore, we explored the total energy within the framework of the PBE pseudopotential of the standardized valley assumption by varying the k-values and cut-off energies of the plane wave. Fig. 2(b) indicates that a k-point mesh of 6 × 6 × 6 is appropriate for this chemical, and an adequate number of k-point samples is required for assessing relative stability. An effective kinetic cut-off range of 50–80 Ry for separating the Mg_3NF_3 material is suggested by the fact that the total energy converges, as shown in Fig. 2(c).

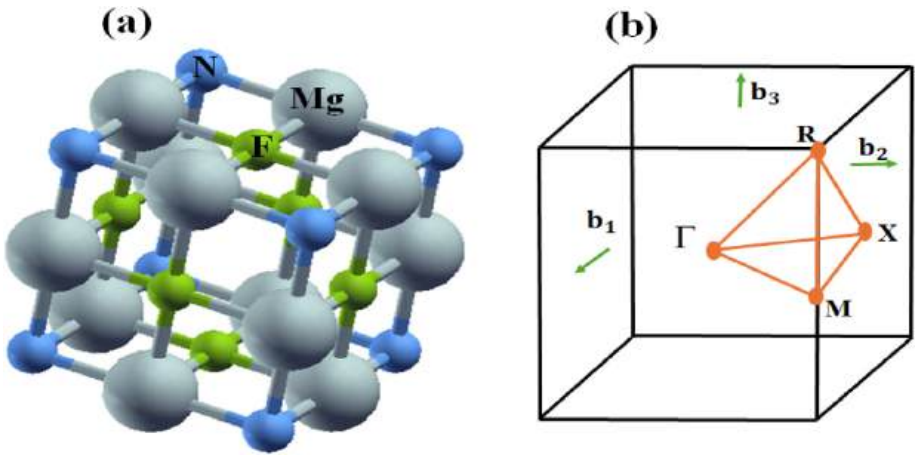

Fig. 1. (a) Optimized structure of Mg_3NF_3, a new inorganic halide perovskite and (b) k-path of the first Brillouin zone for determining electronic band structure.

Table 1
Mg_3NF_3 material lattice constant and energy bandgap were determined using investigational data using DFT calculations.

Structure	Lattice Constant (A°)	This work Bandgap Energy (eV)		Previous work Bandgap Energy (eV)	Previous work experimentally Bandgap Energy (eV)
Mg_3NF_3	4.34	2.98 (PBE)	5.36 (HSE)	5.73 (HSE) [90]	3.6[91]

3.2. Electronic properties

An energy band profile study is crucial to comprehending the materials' electrical activity and optical response. The GGA method, as shown in Fig. 3, is implemented to assess the energy bandgap of unexplored compounds. Within the Brillouin Zone (BZ), the energy value is stretched out over a wide range, from −5 to +5 eV, in a direction of high symmetry. In the image that follows, the dashed line symbolizes the Fermi energy level, and the alphabetic letters indicate the high equilibrium points of irreducible BZ. The direct band, embodied in Mg_3NF_3, is situated at the Γ(gamma) symmetric points, which are additionally the locations of the valence band maxima (VBM) and conduction band minima (CBM), as shown in Fig. 3(a). A bandgap value of 2.98 eV is anticipated for Mg_3NF_3 structures via the PBE function and a bandgap value 5.36 eV is anticipated via the HSE function. We observe that for PBE function calculation bandgap is decreasing than HSE function.

Both LDA + U and LDA approaches are subject to the bandgap underestimating restrictions. Contrasting the GW approach with hybrid functional are two of the many approaches that researchers have devised to fix bandgap calculation errors. Nevertheless, there are restrictions with these methods [50]. The GGA + U technique alters the theoretically estimated bandgap somewhat compared to the empirically measured value. Nayak et al. [51,52] found that the PBE approach accurately predicts band structure and bandgap changes caused by strain, regardless of the function used. The results indicate that the PBE/GGA functional is suitable for investigating strains in materials. Direct bandgap crystalline materials are ideal for photovoltaic, optoelectronic, and photothermal uses [39,50,53,54].

Partial density of states (PDOS) often illustrates the contribution of each several atom as well as its different states to the bandgap energy of the Mg_3NF_3 structures. For the Mg_3NF_3 structures, Fig. 3(b) displays the distribution of PDOS throughout the energy range of −5 to 5 eV. A noteworthy feature of Mg_3NF_3 is that its hybridized states of N and Mg with F preserve the bandgap over the whole energy spectrum. Primary covalent bonds are what bind Mg-F and N-F together. Moreover, the strong differences in atomic states in the Mg_3NF_3 structure causes the electron charge to go from Mg and N to F. In the region surrounding the Fermi level, the Mg^{2+} atoms have a negligible impact. The F-5p orbital has a significant impact on the density of states (DOS) close to the valence band of Mg_3NF_3, as we discovered while analyzing the cubic phase. In contrast, the Mg-4s orbitals have very little influence over the conduction band, which is generally governed by the N-3p orbital.

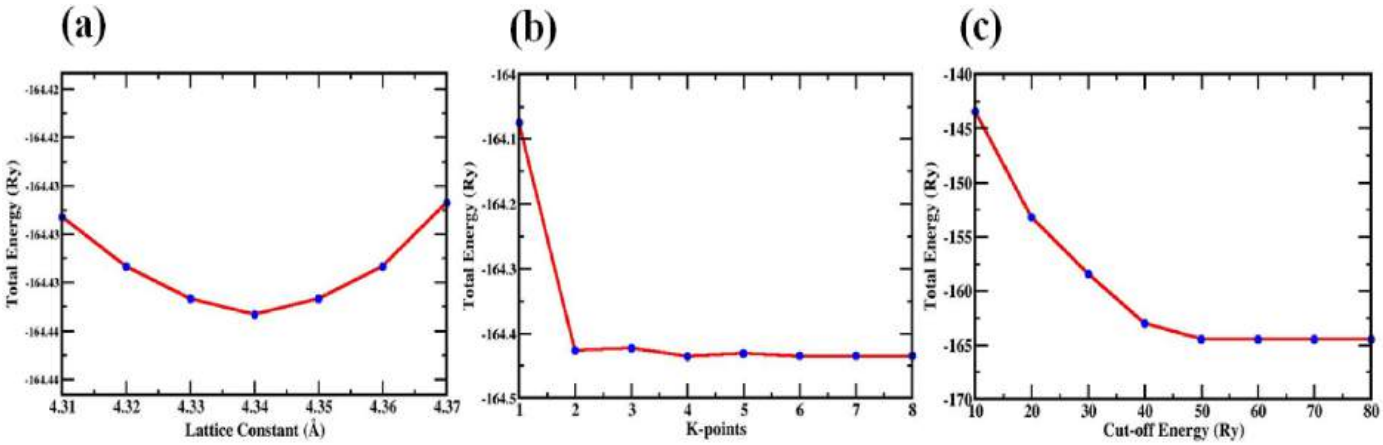

Fig. 2. Adjustment in Mg_3NF_3 per unit cell total energy with respect to (a) lattice constant, (b) k-points and (c) cut-off energy.

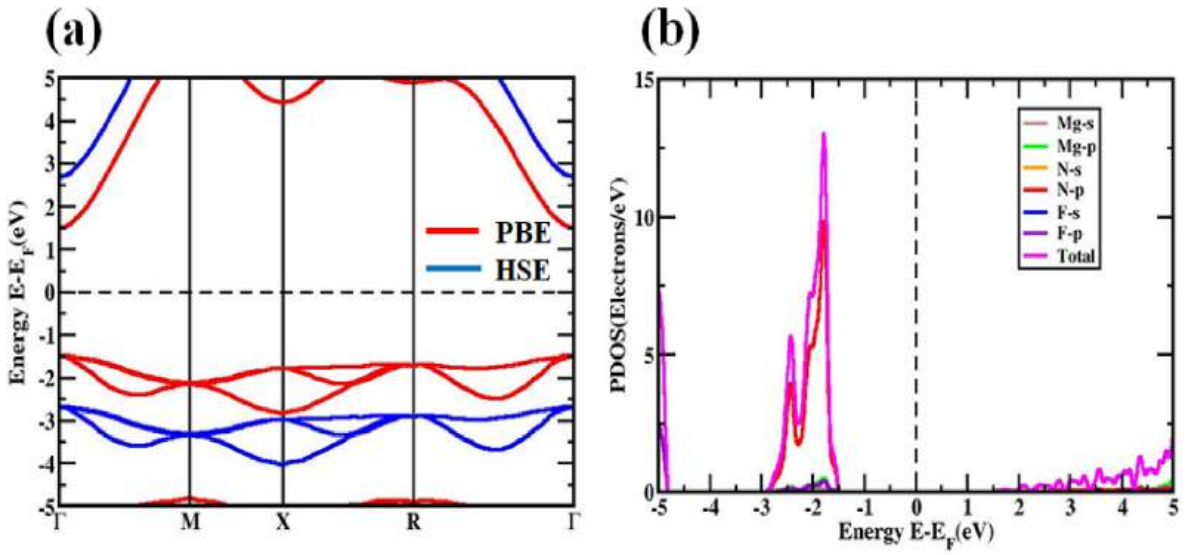

Fig. 3. Without SOC, the Mg_3NF_3 perovskite structure exhibits (a) an electronic band formation, (b) shows partial density of states (PDOS).

3.3. Structural stability

When dealing with phonons in a crystal lattice, the relationship between momentum and phonon energy is referred to as "phonon dispersion". Phonons, which are quantized vibrations of a material's lattice, influence its mechanical and thermal properties as they travel. The lattice volume and atomic positions are loosened during the phonon estimate [55,56]. The phonon band of the Mg_3NF_3 molecule is shaped by the initial Brillouin zone, which runs along the high-symmetry domains Γ-M-X-R-Γ. Fig. 4(a), the dispersion mapping, must be explored to determine the substance's long-term stability. The absence of negative proximity frequencies in the dynamic matrix is evident by this map. For both compressive and tensile strain the phonon structure are illustrated in Fig. S1. From Fig. S1. We observe that for both compressive and tensile strain the compound is stable.

Several studies using ab initio molecular dynamics (AIMD) simulations have concentrated on compounds used in solid electrolytes [55–57]. The highly occupied component of the well-known solid electrolyte material Li_6PS_5Cl (argyrodite)[58–66] raises concerns while building the input model framework for DFT and AIMD calculations. AIMD models may be used to study the effects of long-range dispersion interactions and how structural factors affect electrical band gaps. Further proof that Mg_3NF_3 is thermally stable can be seen in Fig. 4(b and c), which displays the outcomes of the AIMD simulations at room temperature (300 K). The temperature and energy statistics seem to exhibit only slight fluctuations over time, with no significant structural change toward the end. Fig. 4(b) shows the total energy vs time interactions, whereas temperature vs time intimacy connection is shown in Fig. 4(c).

3.4. Charge density

A component's electronic charge density is a key metric for evaluating its electrical features. A precise visualization of the overall charge concentration may be obtained by sketching a charge density map of the valence electrons in a unit cell. By evaluating the entire electronic charge density map, scientists can deduce a molecule's chemical bonding. Structured atoms' charge density curves illustrate the impact of orbital electron accumulation on electrical properties of the atoms.

Fig. 5(a) depicts a two-dimensional map that connects the (200) crystallographic plane to the charge density of Mg_3NF_3. The color scale bar on the right side of the image indicates the strength of electron density, with different hues representing increasing intensities. Fig. 5(b) depicts a three-dimensional charge distribution. On the charge density diagram, the nitrogen atom (N) cannot be identified separately due to the overlapping charges of the magnesium atom (Mg). The formation of a covalent connection between the Mg and N ions is demonstrated by

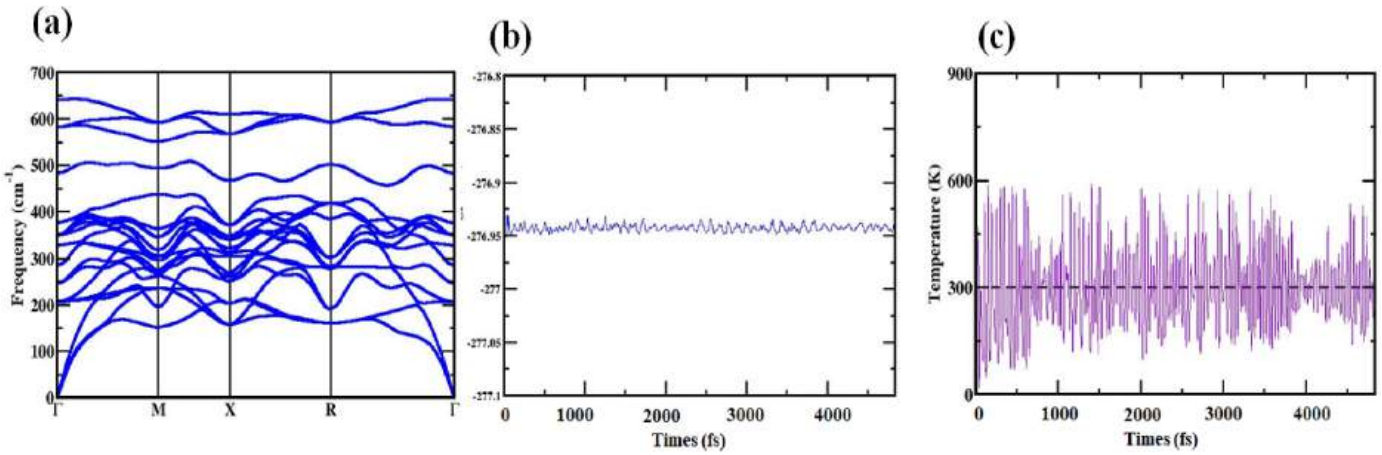

Fig. 4. (a) Mg_3NF_3 compound's phonon band structure; (b) the total energy variation over time and (c) the temperature variation over time of the Mg_3NF_3 material during the AIMD simulation.

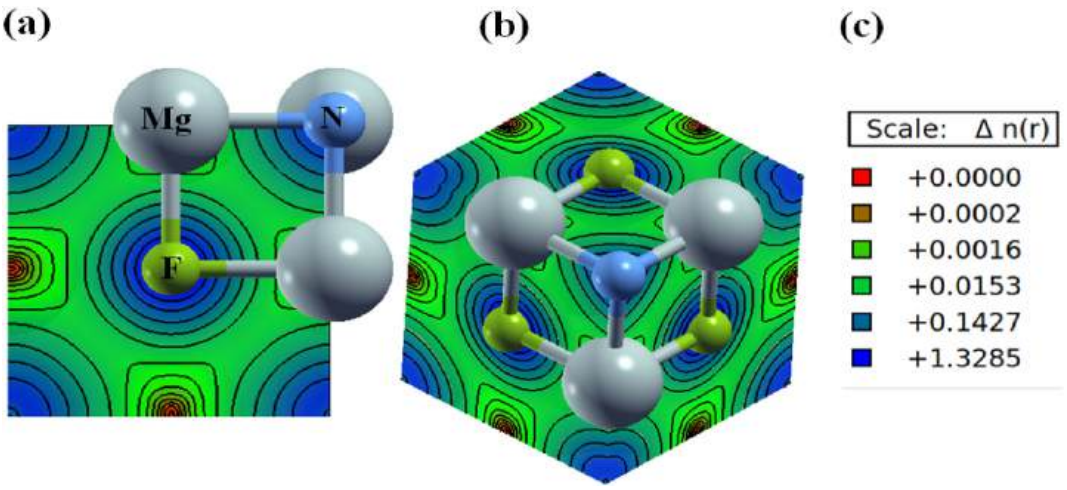

Fig. 5. Charge arrangement in Mg_3NF_3 (a) regarding the (200) plane in 2D and (b) in 3D viewpoint, (c) color scale bar.

this [67,68]. Regarding the idea of an ionic connection between Mg and F ions, non-coincidental charge contours on the charge distribution map offer additional evidence [67,69]. In contrast to the weaker covalent interaction between Mg and F ions, the process of ionic bonding enhances binding inside the structure. In contrast, N and F atoms exhibit antibonding properties.

3.5. Effect of SOC on electronic structure

We factored in the Hamiltonian equation employing SOC with the goal of exploring the consequence of SOC on the electrical characteristics of the Mg_3NF_3 perovskite [70],

$$H_{soc} = \frac{\hbar}{4m_0c^2}\left(\vec{F} \times \vec{p}\right)\cdot\vec{s}. \quad (2)$$

The Hamiltonian operator that considers SOC is marked by H_{soc}, where $\hbar$ is the reduced Plank's constant, p→ stands for orbital angular momentum, F→ is the force or potential energy, m_0 is the mass of unbound electrons, and s→ is the spin angular momentum. We assessed the relativistic effect magnitude and evaluated the effects of the heavy elements Mg and N on the SOC-included electronic structures of Mg_3NF_3 perovskites using relativistic calculations using the PBE functional approach. Viewed in Fig. 6(a) and (b) are the changes to the CBM and VBM positions caused by the significant impact of SOC on the conduction and valence band areas. In contrast, Mg_3NF_3's bandgap energy value is 3.24 eV due to the SOC. The SOC effect causes a bandgap value rise in Mg_3NF_3 perovskite structures. Fig. 6(a) shows this shift in the bandgap.

To have a better grasp of the band development of cubic Mg_3NF_3, it could be worthwhile to study the PDOS while factoring the effect of the SOC. When SOC is thinking about, the unique electron effect changes the conduction and valence bands in comparison to PDOS when SOC is omitted. In the existence of SOC, the PDOS, as shown in Fig. 6(b), does not reveal any pattern in its impact on the Mg atoms. At regions with great symmetry, the band edge separation caused by the SOC effect does not manifest as F-5p into p (j = 1/2) and F-5p into p (j = 3/2) splitting apart. In the VB, the energy spectrum of −5 to 1.6 eV is mostly influenced by the F-5p (j = 1/2) and F-5p (j = 3/2) atoms, as seen in Fig. 6(b). Contrarily, N-3p (j = 1/2) and N-3p (j = 3/2) are mostly responsible for the energy on the CB portion, which spans from 1.6 to 5 eV.

3.6. Strain-driven by electronic properties

The impact of surface area ratio (SOC) on compressive and tensile stresses on the configuration of Mg_3NF_3 with and without SOC is assessed using strain as a percentage. Compressive to tensile strain is

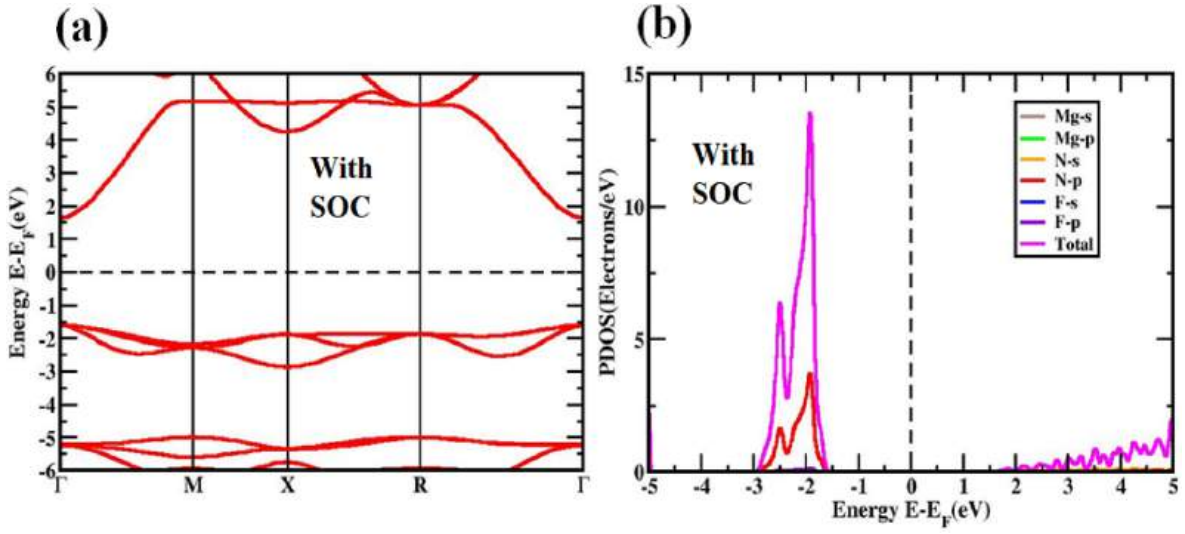

Fig. 6. (a) Band structure and (b) PDOS employing the PBE function of the proposed Mg_3NF_3 structure with SOC impact.

intended to be calculated in 1 % steps across a pressure range of −3% to +3 %. According to Fig. 7(a), when compressive and tension strain are applied to perovskites containing concentrations of Mg_3NF_3, the VBM and CBM approach the Fermi zone. The band topologies of Mg_3NF_3 that bear the SOC impact while feeling tension and compression strain concurrently are seen in Fig. 7(b). After accounting for the SOC impact, the compressive strain widens the connection between the Mg_3NF_3 atoms, packing more orbits into a given area.

At Γ-point for Mg_3NF_3, the locations of the VBM and CBM seem to be quite important when compressive strain is applied. These positions range from −3% to 0 %. The Γ-point yields the linear bandgap for Mg_3NF_3, whatever the application of the SOC impact. The bandgap is demonstrated to have developed both within and outside of the SOC impact because to a rise in compressive strain. Further altering the composition of the electrical band is a tensile strain applied in the region of 0 % to +3 %. Because tensile strain has been included, the VBM and CBM for these situations have deviated from the Fermi level. Under tensile tension, the band gap narrows in the Mg_3NF_3 structures. A linear bandgap at the Γ-point has been found after a thorough investigation of the SOC effect in the Mg_3NF_3. In the Mg_3NF_3 combination, compressive, and tensile strain result in a direct bandgap in the electrical band arrangement. Table 2 and Fig. 8, in turn, show the bandgap deviations for the Mg_3NF_3 materials during compressive and tensile consumption, with and without the SOC effect. The bandgaps of Mg_3NF_3 were found to vary in the utilized strain range of −3% to +3 % from 3.513 to 2.536 eV (without using SOC) and 3.816 to 2.755 eV (with SOC). The parameters of the indirect bandgap for Mg_3NF_3 is unexpectedly unchanged during the complete applied strain limit. Thus, Shockley-Queisser's hypothesis [71] may be able to be used by these structures to increase the productivity of solar cells.

The TDOS for Mg_3NF_3 in various configurations, both with and without the interaction of SOC and biaxial strain, is shown in Fig. 9. TDOS analysis is extremely helpful in improving our understanding of the dynamics of the electronic band structure in Mg_3NF_3. The valence band, which is primarily controlled by the F atom's orbitals, accords with the Fermi level in the unstrained Mg_3NF_3 in TDOS and is unaffected by the presence of SOC. The orbitals of Mg-3p and N-3p have little bearing. Furthermore, the presence of SOC does not significantly alter the TDOS of the conduction band due to the N atomic orbitals; but the Mg-3p and -5p orbitals and the Fermi level do. According to what Nayak et al. found, there is no DOS proximity line to the Fermi level, indicates the bandgap and semiconductor properties of the material. It has not been possible to find any connection between this impact and the functional exchange coefficient utilized [72].

The TDOS line appears at the Fermi level as the consequence of compressive stresses between 0 % and −3%. For Mg_3NF_3 materials, the conductivity drops despite whether the SOC effect remains unchanged because the TDOS line is higher than the Fermi level during tensile strain ranging from 0 % to +3 %. It is expected that the bandgap will change following an extensive review of the band arrangement and DOS of the Mg_3NF_3 materials.

Table 2
The calculated bandgap of cubic Mg_3NF_3 perovskite under different compressive and tensile strains.

Applied Strain (%)	Mg_3NF_3			
	Compressive		Tensile	
	Without SOC	With SOC	Without SOC	With SOC
0	2.982	3.245	2.982	3.245
1	3.157	3.436	2.830	3.086
2	3.336	3.628	2.656	2.919
3	3.513	3.816	2.536	2.755

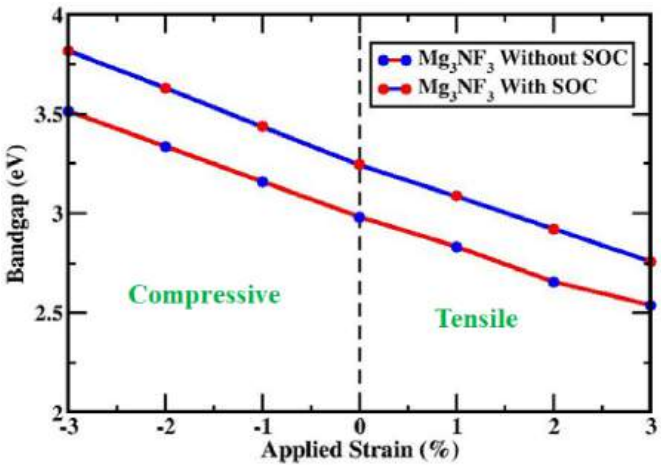

Fig. 8. The change in the bandgap of the Mg_3NF_3 electronic band structure with biaxial strain, both with and without the SOC effect.

3.7. Optical properties

It is important to analyze the optical characteristics of the materials, including absorption, dielectric behavior, and loss function to determine whether they are suitable for use in optoelectronic applications. By

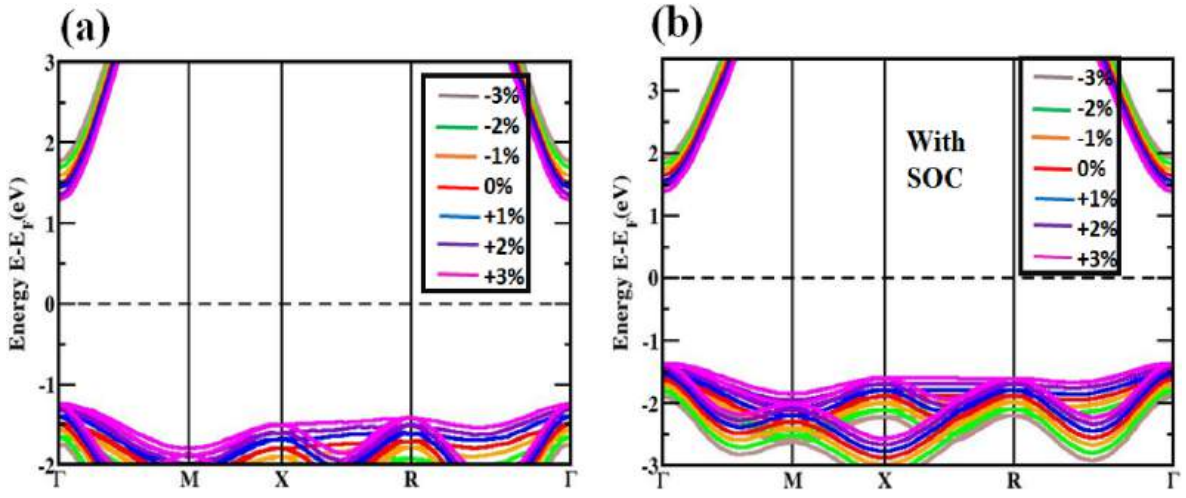

Fig. 7. A structure of the electronic band of Mg_3NF_3 under different strain (a) without and (b) with SOC effect.

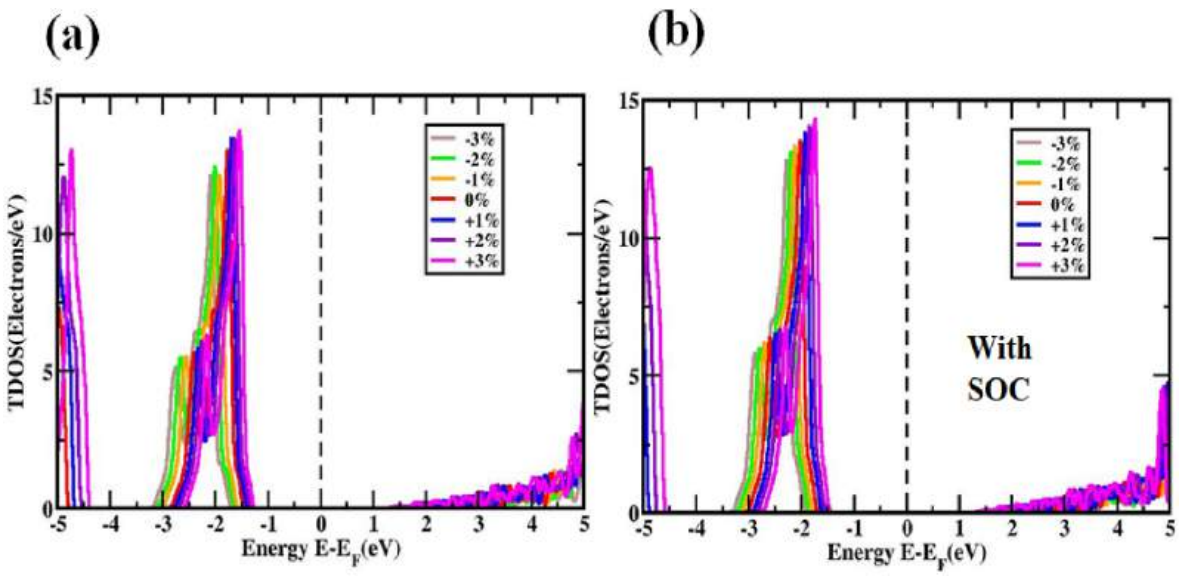

Fig. 9. TDOS of Mg_3NF_3 at various compressive and tensile strains (a) without and (b) with the SOC effect.

injecting biaxial strain to change the lattice parameter, we may improve the optical attributes of the material. The absorption coefficients give important information about how far light penetrates a material's surface before being absorbed when a certain wavelength of light interacts with it. These coefficients are important in many different contexts, one of which is cellular systems. This study looked at the various characteristics of Mg_3NF_3 and it was discovered that these properties could be changed by applying biaxial compression (from 0 % to −3%), as well as tensile stresses (from 0 % to +3 %). Dielectric operations, extinction loss factor (EELF), reflectivity, and absorption coefficients are important optical attributes of materials for utilization in optoelectronics and solar cells.

The dielectric performance is dependent on the frequency, ω, of the incoming light for both the real element ε_1 (ω) and the imagined component ε_2 (ω). By using the Kramers-Kronig transformation, the real dielectric function is discovered. In addition, as mentioned in Ref. [73], the unreal dielectric function is ascertained by utilizing the components of the momentum matrix. The material's EELF and absorption coefficient in equation (3) may be determined using the critical portion of the dielectric function ε_1 (ω) for the Mg_3NF_3 perovskite [54,74].

$$\varepsilon_1(\omega) = 1 + \frac{2}{\pi} P \int_0^{\infty} \frac{\varepsilon_2(\omega')\omega'}{\omega'^2 - \omega^2} d\omega \tag{3}$$

where P is the absolute prime number.

Additionally, the hypothetical dielectric activity ε_2 (ω) is obtained through equation (4) [54,74]

$$\varepsilon_2(\omega) = \frac{Ve^2}{2\pi\hbar m^2\omega^2} \times \int d^3k \sum |\langle \varphi_c | p | \varphi_v \rangle|^2 \ \delta(E_c - E_v - \hbar\omega) \tag{4}$$

The unit cell's volume is represented by V, Planck's constant is expressed in compact form as $\hbar$, the motion is denoted by the operator p, and the valence and conduction bands that match the wave functions are often designated as ϕ_c and ϕ_v.

The absorption coefficient $\alpha(\omega)$ may be found by combining the real and unreal components of the dielectric operation. Formula (5) is used to estimate the absorption coefficient [54,74].

$$\alpha(\omega) = \frac{\sqrt{2}\omega}{c} \left[\sqrt{\varepsilon_1(\omega)^2 + \varepsilon_2(\omega)^2} - \varepsilon_1(\omega)\right]^{1/2} \tag{5}$$

where c symbolizes the quickness of light.

Based on equation (6), the dielectric parameter $\varepsilon(\omega)$ is composed of two parts: the real part, ε_1 (ω) and the imaginary part, ε_2 (ω) [73]. Parts of the momentum matrix are implemented for identifying the imaginary section of the dielectric property, while the Kramers-Kronig revision is used to gain the real part [75,76]

$$\varepsilon(\omega) = \varepsilon_1(\omega) + i\varepsilon_2(\omega) \tag{6}$$

Concerning photon energies up to 20 eV, Fig. 10(a) displays the real components of the strained and unstrained Mg_3NF_3 dielectric constants. The relationship between scatter effects and polarization has been clarified by utilizing the real element of the dielectric function. A material's electronic portion of the dielectric function, represented as ε_1 (0), occurring at zero frequency, must be considered to comprehend its ocular properties. To cubic Mg_3NF_3, ε_1 (0) is assigned a value of 3.14. The dielectric function's real portion, ε_1 (ω), exhibits a trend as it rises from ε_1 (0) to its maximum value. It's noteworthy that distinct peaks of absorption develop at photon energies of around 4.42 eV for Mg_3NF_3 in the true portion ε_1 (0) of the dielectric function. Once that's settled down, it creates many peaks. Depending of the applied biaxial strain, the dielectric constant peaks of Mg_3NF_3 display different colors. Because of a narrower bandgap and a bigger peak dielectric constant, the structure showed a redshift with regard to lower photon energy when the tensile strain increased the Mg_3NF_3. Alternatively, Mg_3NF_3 saw a blueshift towards higher photon energy due to an increase in peak dielectric constant with increasing compressive strain.

In Fig. 10(b), the unreal dielectric constants ε_2 (ω) can be observed moving under both strained and unstrained conditions. We have been provided with information about the electrical bandgap via the imaginary dielectric constant ε_2 (ω). For Mg_3NF_3, the values of ε_2 (ω) identify a wide variety of absorption spectra. Fig. 10(b) illustrates that when no strain is applied, the primary peak for ε_2 (ω) is detected at a photon energy of 9.05 eV at the optical maximum level of 3.39. Due to strain, the imaginary portion of the dielectric function's peak climbs abruptly and enters the low-energy region. The imaginary section of the dielectric characteristic is zero for all strain-modulated Mg_3NF_3 samples for photon energy larger than 20 eV. Due to the lack of ε_2 (ω) higher than 20 eV, the strain-modulated samples in this area show excellent optical transparency and very low optical absorption. Peaks in the dielectric constant's imaginary area show the change from the valence to the conduction spectrum. As modifications undergo to the bandgap energy and lattice stability, the placements of the peaks modify. The redshift emerged at lower photon energies when the ensuing tensile stresses

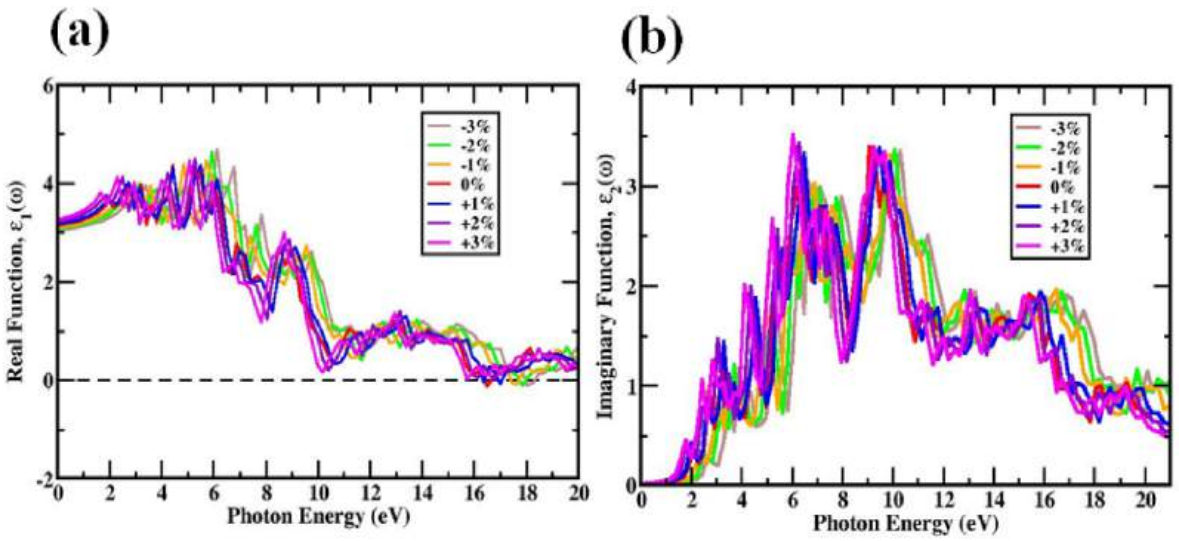

Fig. 10. The dielectric constants, (a) real and (b) imaginary, in relation to various biaxial strains.

were at their highest, while the blueshift occurred at higher photon energies when the resulting compressive strains were at their highest. The results suggest that biaxial tension and compression have a substantial impact on the absorption spectra of Mg_3NF_3 throughout an extensive spectrum of energies.

The optical absorption coefficient of a substance is used to determine how much light it can absorb. The information a solar cell provides can be used to enhance its PCE. Optical absorption coefficient and imaginary part of dielectric function both follow the same pattern in this situation. The optical absorption patterns of Mg_3NF_3 show the greatest peak in the visible spectrum. The absorption coefficient of Mg_3NF_3 under various biaxial strains and unstrained conditions is shown in Fig. 11(a) as a function of photon energy. The absorption pattern indicates that the edge shows a large blueshift in compressive strain and a large redshift in tensile tension. Contrary to their unstrained counterparts, structures subjected to compressive strain have superior visible light absorption properties. The predicted bandgap is proportional to the strain-modulated absorbance change of Mg_3NF_3. The Mg_3NF_3 structure's apparent absorption coefficient increases as compressive strain is elevated, a critical feature for application in solar cells. Mg_3NF_3 apparent absorption coefficient decreases with increasing tensile strain.

The electron loss function may be used to calculate the energy of electrons moving over a dielectric. Equation (7) [73] provides a representation of it.

$$L(\omega) = \frac{\varepsilon_2(\omega)}{\varepsilon_1^2(\omega) + \varepsilon_2^2(\omega)} \tag{7}$$

The energy loss mechanism, or L(ω), is a crucial instrument for investigating a material's reaction to light. It generates energy passage loss inside the material or barrier. As can be witnessed from the peaks in the L(ω) graphs for Mg_3NF_3, energy loss arises as the incoming photon energy approaches the material's bandgap. Fig. 11(b) shows the L(ω) peaks for the cubic framework of Mg_3NF_3 when strain is absent, which is seen between 15.5 eV and 16.31 eV. Dispersions of energies below the bandgap are hard to see. There is a loss function for strain-induced Mg_3NF_3 up to 17.68 eV for photon energy. Fig. 11(b) shows the optical loss of Mg_3NF_3 in various compressive and tensile strain scenarios. Tensile strain induces a redshift in optical loss, which means that all structures migrate toward lower photon energies. But when compressive strain arises, the optical loss reveals a clear blueshift towards higher photon energies.

The reflectivity of the Mg_3NF_3 perovskite material dictates how

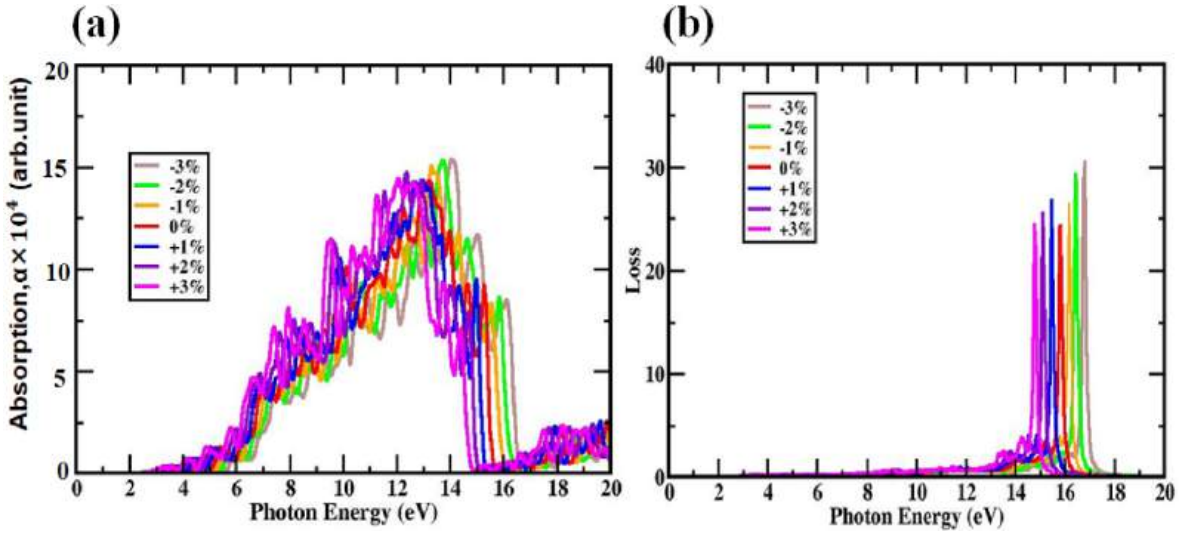

Fig. 11. Regarding both compressive and tensile strains, (a) the absorption coefficient and (b) the loss function as a function of photon energy.

much sunlight either visible light or electromagnetic radiation it can reflect. Three of the numerous variables that can have a substantial effect on the entire reflectivity of perovskites are composition, crystal structure, and surface shape. The Mg_3NF_3 perovskites can exhibit variable reflectances according to the angle and wavelength of light reflection. Photon energy may be derived from the reflectance of the Mg_3NF_3 perovskite material, as shown in Fig. 12(a). Between 0 and 20 eV is where the reflectivity modifications are most noticeable in intensity. The maximum reflection occurs at 9.97 eV for +3 % strain and when no strain is applied the peak occurs at 16.50 eV of energy.

Our findings on the observable features of Mg_3NF_3 is reported here [77], in agreement with other studies. For deployment in visible light devices, materials containing bandgaps less than 3.1 eV are preferable [73]. Among many other potential uses, Mg_3NF_3 perovskite's unique spectrum attributes make it a desirable material for use in solar cells, optoelectronics, and optical sensors. A material's permeability to incoming photons is quantified by its dimensionless refractive index, which quantifies the speed at which light streams through the material. Equation (8) may be employed to get the real component of a material's complex refractive index n(ω).

$$n(\omega) = \sqrt{\frac{\varepsilon_1(\omega)^2}{2} + \sqrt{\frac{\varepsilon_1(\omega)^2 + \varepsilon_2(\omega)^2}{2}}} \tag{8}$$

To ascertain the quantity of light that can flow through the Mg_3NF_3 materials. The n(ω) refraction spectra are displayed in Fig. 12(b). These materials are optically persistent, as demonstrated by the photon energies appearing to hang unchanged above the band gap energy predicted by the refractive index, n. An essential physical property for semiconductors is the static refractive index, or n(0). The static refractive index has a maximum n(0) that is about 5.26 eV when compared to Mg_3NF_3. As energy levels rise, the refractive index of Mg_3NF_3 falls. Even yet, when the energy of the incoming photon reaches E = 16.52 eV, the refractive index decreases to its minimal value, n = 0.70. Owing to the refraction spectrum analysis, this Mg_3NF_3 seems to have distinct refraction indices. These results confirm the experience as planned.

For the Mg_3NF_3 perovskite, the extinction coefficient, K(ω), may be derived using the estimated values of $\varepsilon_1(\omega)$ and $\varepsilon_2(\omega)$ using the relation shown below [78].

$$k(\omega) = \sqrt{\sqrt{\frac{\varepsilon_1(\omega)^2 + \varepsilon_2(\omega)^2}{2}} - \frac{\varepsilon_1(\omega)^2}{2}} \tag{9}$$

Referencing the GGA approximations, Fig. 13 illustrates the variations in the extinction coefficient with respect to energy in units of (eV). No value between 0 and 0.68 eV is recorded due to the extinction coefficient's existence in the energy gap area. After the extinction coefficient varies with increasing energy in the range of 0.68–20 eV. The extinction coefficient reaches its maximum value at 10.90 eV. However, we observe that the extinction coefficient progressively varies, sometimes increasing and sometimes reducing, reaching its greatest value in the fundamental absorption zone, where it is predicted to be 1.04 Light's behavior at the semiconductor level is what causes this oscillation [79].

3.8. Mechanical properties

To measure the stability and stiffness of a material, one may look at its elastic constant, which is an essential quality for rigid materials. A crystal's resistance to biaxial strain may be precisely determined by its elastic constant. Understanding the mechanical characteristics of Mg_3NF_3 structures requires evaluating the implications of stress on their elastic constants. Three prominent elastic constants, C_{11}, C_{12}, and C_{44}, are found in the Mg_3NF_3 structure in this DFT research using a variable halide ratio. One parameter that estimates a substance's ductile and flexible qualities is the Cauchy pressure, which is based on the C_{12}-C_{44}

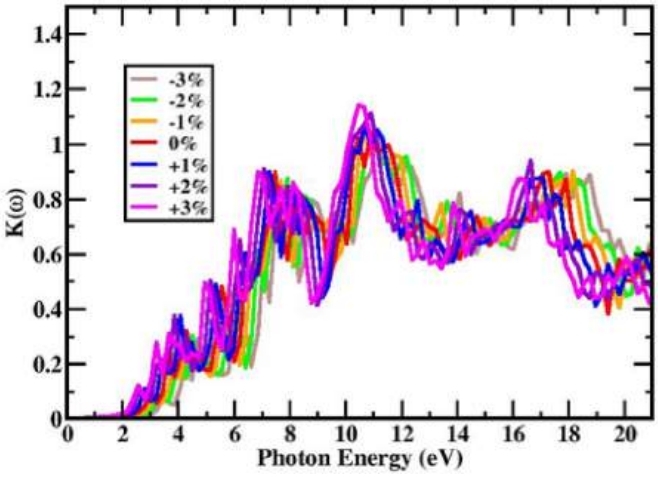

Fig. 13. Extinction coefficient of Mg_3NF_3 under compressive and tensile strains.

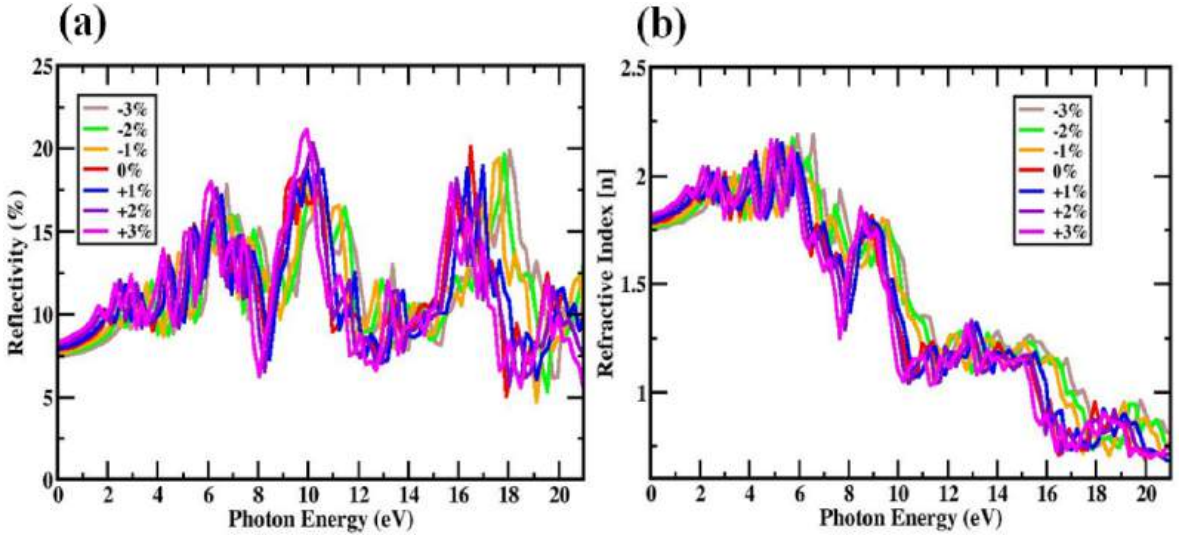

Fig. 12. (a) Reflectivity, (b) Refractive index [n] of Mg_3NF_3 under compressive and tensile strains.

value. The popular Born stability specifications listed below are standard procedures for assessing the mechanical steadiness of the Mg_3NF_3 materials:

$$C_{11} > 0, C_{44} > 0, C_{11} + 2C_{12} > 0, C_{11} - C_{12} > 0$$

This ductile state is indicated by a positive Cauchy pressure. To distinguish between ductile and brittle components, Pugh et al. [80,81] introduced the classic formula, Pugh's ratio. It is the ratio of the shear modulus (G) to the bulk modulus (B) of 1.75 and is referred to as the crucial value of B/G. In conclusion, ductile materials possess a ratio above 1.75, while fragile materials likely have a ratio less than 1.75. The calculated values in Table 3 indicate that the compound Mg_3NF_3 is ductile.

Multiple anisotropy indices can be used to characterize the directionally dependent aspects of a system. Solids are anisotropic due to the innate asymmetry and orientational preferences of individual molecules. For example, studying elastic anisotropy for systems subjected to various degrees of external stress has several applications in crystal physics and engineering, which improves mechanical durability [82–84]. The subsequent formula (10) [85]:

$$A^U = 5\frac{G_V}{G_R} + \frac{B_V}{B_R} - 6 \geq 0 \quad (10)$$

Ranganathan et al. and Shiva Kumar proposed the A^U (universal anisotropic index). An isotropic condition of a material may be stablished by calculating its universal anisotropy (A^U) value. The estimated A^U value for Mg_3NF_3 shows anisotropic behavior, which differs from the isotropic behavior of a material when $A^U = 0$. Mg_3NF_3 deviates the most from zero of the minerals investigated.

The following formula (11, 12) can be used to estimate the fraction of anisotropy under shear (A_G) and bulk (A_B) conditions.

$$A_G = \frac{G_V - G_R}{G_V + G_R} \quad (11)$$

$$A_B = \frac{B_V - B_R}{B_V + B_R} \quad (12)$$

The subscripts B and G represent the bulk and shear moduli, respectively, using the Voigt and Reuss approximations (V and R), respectively. As stated in Ref. [86], the elastic anisotropy of the material reaches its greatest when $A_B = A_G = 1$ and its minimum when $A_B = A_G = 0$. The measured value of A_G indicates that the material in question has an isotropic bulk modulus, which implies that the shear anisotropy that exists currently is real. By investigating and assessing shear anisotropy in various orientations at different crystallographic planes, more accurate insights into elastic anisotropy have been discovered. The following equations (13)–(15) define the shear anisotropic factors A_i, where i is a number between 1 and 3 [86,87].

For {100} shear plane,

$$A_1 = \frac{4C_{44}}{C_{11} + C_{33} - 2C_{13}} \quad (13)$$

For {010} shear plane,

$$A_2 = \frac{4C_{55}}{C_{22} + C_{33} - 2C_{23}} \quad (14)$$

For {001} shear plane,

$$A_3 = \frac{4C_{66}}{C_{11} + C_{22} - 2C_{12}} \quad (15)$$

To get precise anisotropy, one must ascertain the Zener anisotropy index (A) and the matching Zener anisotropy (A^{eq}). By entering them into this equations 16 and 17 [88], we may determine their value:

$$A = \frac{4C_{44}}{C_{11} - C_{12}} \quad (16)$$

$$A^{eq} = \left(1 + \frac{5}{12}A^U\right) + \sqrt{\left(1 + \frac{5}{12}A^U\right)^2 - 1} \quad (17)$$

An A = 1 and the equation $A_1 = A_2 = A_3 = A$ demonstrate the isotropic nature of a cubic structure. Furthermore, this value's distribution indicates the degree of anisotropy. Table 4 illustrates the anisotropic behavior of the material, which is most prominent and has the biggest divergence. The A^{eq} provides additional evidence supporting its nature.

The anisotropy is displayed in Fig. 14(a, b, c) which shows the three-dimensional (3D) framework for the direction dependency of the Young modulus (E) notion of the shear modulus (G) and the Poisson ratio (ϑ), respectively. This crystal is anisotropic, meaning that it is not spherically shaped like an isotropic crystal, which is oriented differently in multiple directions. These results also follow the previous discussion with several markers of anisotropy and Fig. 14(a, b, c) clearly shows that the superconductor material is anisotropic.

3.9. Thermal properties

When studying heat and pressure characteristics at elevated temperatures, a quasi-harmonic Debye approximation is required. The structural parameters may be identified by first applying this fixed estimate to the basic cell volume (E-V) total energy at T = 0 and P = 0. By using the established thermodynamic relationships, the macroscopic attributes are therefore specified in terms of T. When calculating thermal characteristics between 0 and 800 K, the quasi-harmonic technique is likewise very accurate. The thermal effect may be seen in Fig. 15(a), which displays the heat capacity C_v. When considering a constant volume, the C_v approaches the limits set by Dulong and Petit, which are 133 J $mol^{-1}K^{-1}$. The C_v rises in direct proportion to T^3 at low temperatures. The dynamics of atomic motions at intermediate temperatures characterize the heat potential, but until recently, detecting this potential required significant investigative testing [80,89]. At a given temperature, the strain of Mg_3NF_3 causes fluctuations in the C_v, displayed in Fig. 15(a).

The Mg_3NF_3 substance's temperature variability is shown in Fig. 15 (b) from 0 K to 800 K. The Mg_3NF_3 structure's maximum thermal entropy is observed at 800 K. Entropy varies even in the presence of strain variations and this study indicates that it increases with temperature. For both compressive and tensile loads, the entropy modifications are

Table 3
Mechanical and elastic properties of cubic Mg_3NF_3 perovskite as estimated under different compressive and tensile strains.

Strain (%)	C_{11}	C_{12}	C_{44}	C_{12}-C_{44}	B (GPa)	G (GPa)	E (GPa)	B/G	ϑ
−3	132.8	52.9	31.3	21.6	82.5	37.8	95.3	2.18	0.347
−2	102.5	47.6	28.1	19.5	64.7	31.1	78.5	2.08	0.338
−1	71.4	39.6	24.3	15.3	54.1	26.6	64.7	2.03	0.319
0	68.9	37.9	21.7	16.2	47.3	24.2	59.3	1.95	0.307
+1	61.1	36.5	20.9	15.6	45.2	23.5	58.6	1.92	0.299
+2	53.3	35.2	20.1	15.1	40.9	21.7	51.4	1.88	0.285
+3	41.7	34.2	19.3	14.9	38.1	20.5	41.3	1.85	0.276

Table 4
Shear anisotropic factors A_i (i = 1–3), Zener's anisotropy index (A), anisotropy in shear (A_G), anisotropy in bulk modulus (A_B), universal anisotropy index (A^U) and equivalent Zener anisotropy (A^{eq}) of Mg_3NF_3 material.

Mg_3NF_3 Compound	A_1	A_2	A_3	A	A_G	A_B	A^U	A^{eq}
Without SOC	0.7834	0.7834	0.7834	1.5669	0.0050	0	0.0281	1.1651
With SOC	0.8112	0.8112	0.8112	1.7129	0.0044	0	0.0237	1.1507

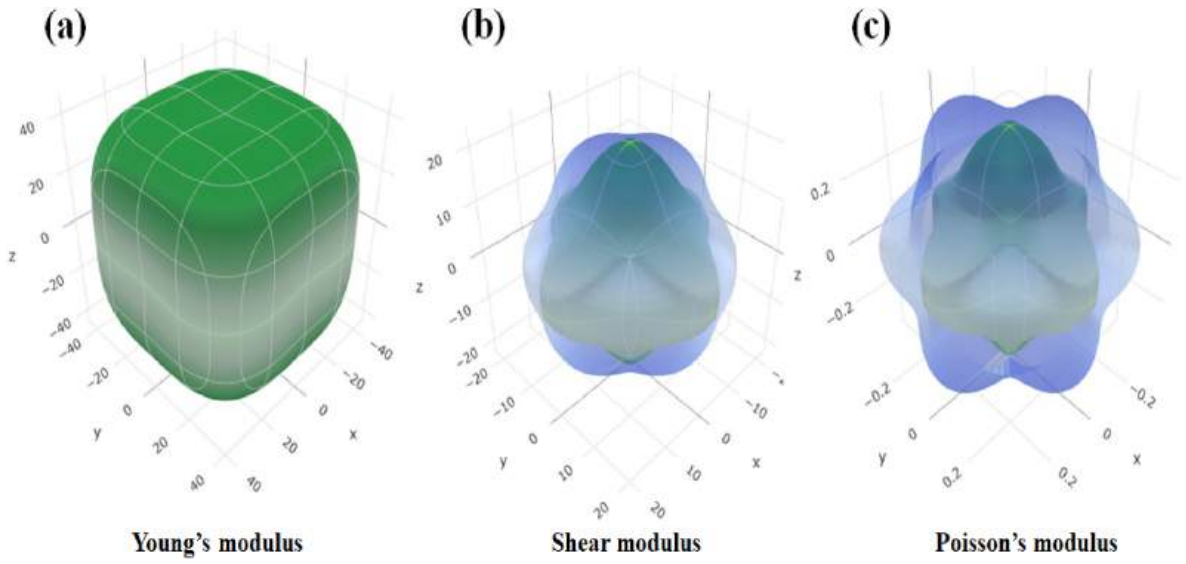

Fig. 14. The isotropy of the Mg_3NF_3 material is shown in (a, b and c) the 3D plots for the following parameters: Young's modulus, E(GPa); Share modulus, G(GPa) and Poisson's ratio, ϑ.

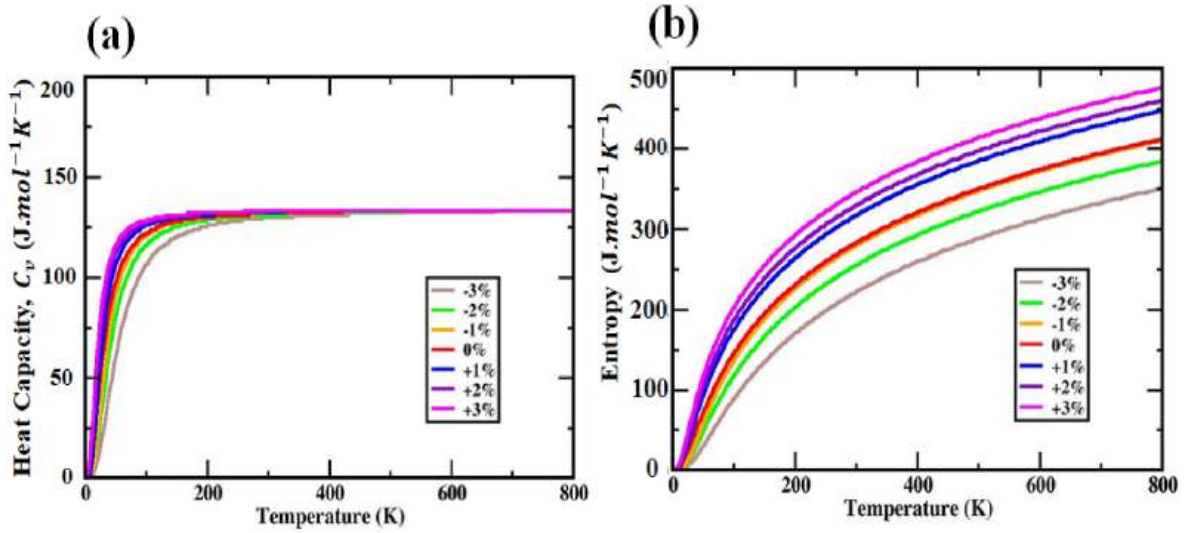

Fig. 15. The material Mg_3NF_3's (a) heat capacity against temperature and (b) the entropy against temperature.

displayed in Fig. 15(b). The maximum entropy is measured at 800 K temperature and for Mg_3NF_3 is 411 J $mol^{-1}K^{-1}$ in the absence of strains. The thermal entropy under strain reaches its greatest at +3 % strain, where it is measured at 475 J $mol^{-1}K^{-1}$. The values for Mg_3NF_3 material that is lowest at −3% strain is 350 J $mol^{-1}K^{-1}$.

The applied strain noted in Fig. 16 causes variations in the Debye temperature υ_D. Increasing compressive strain causes the Debye temperature to rise while increasing tensile strain causes the Debye temperature υ_D to fall. The highest Debye temperature υ_D occurs at −3% strain, while the minimum Debye temperature υ_D occurs at +3 % strain.

The Debye temperature υ_D of Mg_3NF_3 is affected by temperature and pressure, as illustrated in Fig. 17. Acoustic excitation is, by far, the most common cause of lattice vibration at temperatures below the material's Debye temperature. However, once the temperature goes above the Debye temperature, this effect is lost.

$$\upsilon_D = \frac{\leftarrow}{K_B}\left(6\pi^2 V^{\frac{1}{2}} n\right)^{\frac{1}{3}} f(\delta)\sqrt{\frac{B_s}{M}} \tag{18}$$

Equation (18) needs the following variables and constants: Boltzmann constant (k_B), adiabatic bulk modulus (B_s), volume (V), molecular

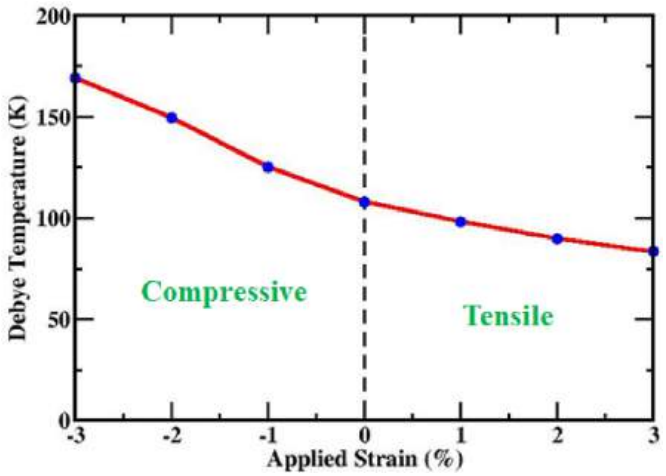

Fig. 16. The Debye temperature of the Mg_3NF_3 compound varies with strain at a constant temperature of 0 K.

mass (M), number of atoms per primitive cell (n), and f(δ), which is a function of Poisson's ratio. Fig. 17(a) demonstrates that υ_D is increasing in a small range as the temperature rises from 0K to 800K when pressure is constant. This characteristic is also maintained in varied pressures. We also discovered that as pressure increases, so does the Debye temperature. Fig. 17(b) depicts the relationship between applied pressure and Debye temperature fluctuations. We conclude that when pressure increases, so does the Debye temperature. This trait persists across temperature ranges.

The chemical potential of perovskites or the propensity of the material's constituents to exchange or react with other substances, does in fact affect the material's thermal stability. The thermal stability and chemical potential of perovskites are closely related. Phase stability, defect formation, decomposition pathways, and overall material stability can all be impacted by changes in chemical potential. The thermal stability of perovskite materials can be enhanced, and their performance can be optimized for a range of applications, by comprehending and managing the chemical potential. From Fig. 18, we can observe that the chemical potentiality has a minor variation with respect to temperature, this minor variation does not create any impact on this material's characteristics (stability). So, we can say this material is thermally stable.

4. Conclusion

Using first-principles density-functional theory simulations, the structural, optical and electrical features of the inorganic perovskite Mg_3NF_3 have been explored. After optimization, the lattice parameters of Mg_3NF_3 were found to be 4.34 A°. A range of strain conditions, from −3% to +3 %, is investigated for the dielectric function, thermal stability, light absorption, loss, and reflectivity characteristics of Mg_3NF_3. Moreover, with tensile strain, the bandgap of Mg_3NF_3 tends to contract and approach the metallic state. Compressive strain, however, causes the bandgap to rise whether the SOC effect is present. The compounds Mg_3NF_3 have a direct bandgap of Mg_3NF_3 is 2.98 eV. The electronic bandgaps of Mg_3NF_3 increase to 3.24 eV when SOC is considered. Electrical, structural, and optical features of Mg_3NF_3 may be altered by biaxial compressive and tensile strain. An understanding of Mg_3NF_3's possible uses in solar cells and electrical components may be gained by taking strain and SOC into account during its identification. Without incorporating the SOC consequences, the bandgap exhibited an increasing trend as tensile tension dropped. Conversely, when the compressive strain is applied, the bandgap exhibits a rising tendency. The peak of the Mg_3NF_3 dielectric constant moves to a higher photon energy as the compressive strain rises, confirming a blueshift. However,

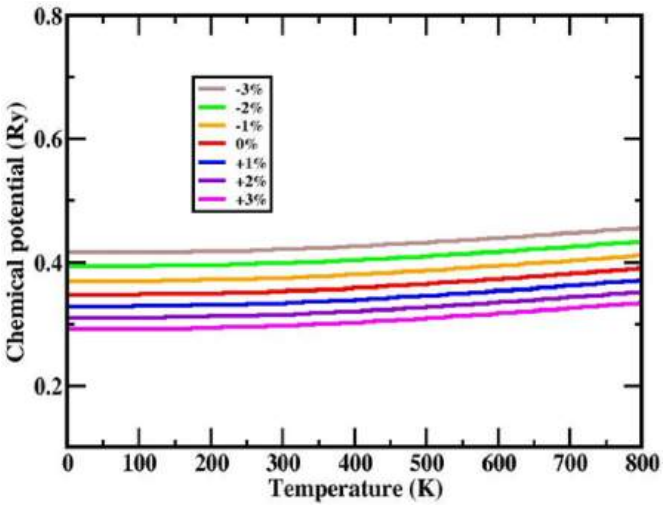

Fig. 18. Chemical Potentiality of Mg_3NF_3 under compressive and tensile strains.

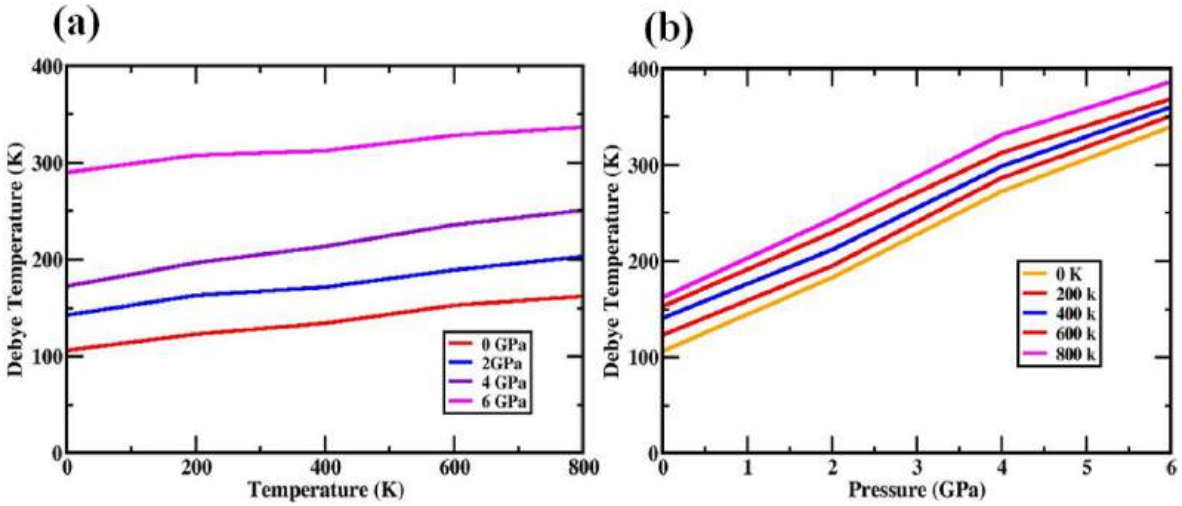

Fig. 17. At a different temperature and pressure, the Debye temperature varies with respect to pressure and temperature for Mg_3NF_3 compound.

a redshift happens as tensile strain increase and the peak of the dielectric constant goes nearer lower photon energy. This finding provides more evidence that the strain-dependent electrical and optical properties of Mg_3NF_3 studied here may be used to the production of optoelectronics and solar cells.

CRediT authorship contribution statement

I.K. Gusral Ghosh Apurba: Writing – original draft, Visualization, Software, Formal analysis, Data curation. **Md. Rasidul Islam:** Writing – review & editing, Writing – original draft, Validation, Supervision, Methodology, Investigation, Conceptualization. **Md Masud Rana:** Writing – review & editing, Validation, Resources, Methodology, Conceptualization. **Jehan Y. Al-Humaidi:** Writing – review & editing, Validation, Software, Project administration, Funding acquisition. **A.M. Quraishi:** Funding acquisition, Investigation, Methodology, Validation, Writing – review & editing. **Parvez Ali:** Funding acquisition, Investigation, Methodology, Validation, Writing – review & editing. **Md. Shizer Rahman:** Writing – review & editing, Visualization, Methodology, Formal analysis, Data curation.

Declaration of competing interest

The authors declare that they have no known competing financial interests or personal relationships that could have appeared to influence the work reported in this paper.

Acknowledgements

This research is funded by Princess Nourah bint Abdulrahman University Researchers Supporting Project number (PNURSP2025R24), Princess Nourah bint Abdulrahman University, Riyadh, Saudi Arabia.

Appendix A. Supplementary data

Supplementary data to this article can be found online at https://doi.org/10.1016/j.physb.2024.416879.

Data availability

Data will be made available on request.

References

[1] G.E. Eperon, G.M. Paternò, R.J. Sutton, A. Zampetti, A.A. Haghighirad, F. Cacialli, H.J. Snaith, Inorganic caesium lead iodide perovskite solar cells, J. Mater. Chem. A 3 (2015) 19688–19695.
[2] H. Zitouni, N. Tahiri, O. El Bounagui, H. Ez-Zahraouy, How the strain effects decreases the band gap energy in the CsPbX3 perovskite compounds? Phase Transitions 93 (2020) 455–469.
[3] P. Pitriana, T.D.K. Wungu, R. Hidayat, The characteristics of band structures and crystal binding in all-inorganic perovskite APbBr3 studied by the first principle calculations using the Density Functional Theory (DFT) method, Results Phys. 15 (2019) 102592.
[4] L. Zhang, T. Hu, J. Li, L. Zhang, H. Li, Z. Lu, G. Wang, All-inorganic perovskite solar cells with both high open-circuit voltage and stability, Front. Mater. 6 (2020) 330.
[5] M.F. Rahman, M.A. Rahman, M.R. Islam, A. Ghosh, B. Shanto, M. Abul, M. Chowdhury, M. Al Ijajul Islam, M.H. Rahman, M.K. Hossain, Unraveling the strain-induced and spin–orbit coupling effect of novel inorganic halide perovskites of Ca3AsI3 using DFT, AIP Adv. 13 (2023).
[6] M.F. Rahman, M.A.I. Islam, M.R. Islam, M.H. Ali, P. Barman, M.A. Rahman, M. Harun-Or-Rashid, M. Hasan, M.K. Hossain, Investigation of a novel inorganic cubic perovskite Ca3PI3 with unique strain-driven optical, electronic, and mechanical properties, Nano Sel (2023).
[7] A. Ghosh, M.F. Rahman, M.R. Islam, M.S. Islam, M. Amami, M.K. Hossain, A.B. Md Ismail, Inorganic novel cubic halide perovskite Sr3AsI3: strain-activated electronic and optical properties, Heliyon 9 (2023) e19271, https://doi.org/10.1016/j.heliyon.2023.e19271.
[8] M.A. Ali, A.A.A. Bahajjaj, S. Al-Qaisi, M. Sillanpää, A. Khan, X. Wang, Structural, electronic, magnetic and thermoelectric properties of Tl2NbX6 (X= Cl, Br) variant perovskites calculated via density functional theory, J. Comput. Chem. 44 (2023) 1875–1883.
[9] R.K. Pingak, S. Bouhmaidi, L. Setti, B. Pasangka, B. Bernandus, H.I. Sutaji, F. Nitti, M.Z. Ndii, Structural, electronic, elastic, and optical properties of cubic BaLiX 3 (X= F, Cl, Br, or I) perovskites: an ab-initio DFT study, Indones. J. Chem. (2023).
[10] S. Bouhmaidi, M.B. Uddin, R.K. Pingak, S. Ahmad, M.H.K. Rubel, A. Hakamy, L. Setti, Investigation of heavy thallium perovskites TlGeX3 (X= Cl, Br and I) for optoelectronic and thermoelectric applications: a DFT study, Mater. Today Commun. 37 (2023) 107025.
[11] T. Jackson, M. Oliver, The viability of solar photovoltaics, Energy Pol. 28 (2000) 983–988.
[12] M.K. Hossain, G.F.I. Toki, D.P. Samajdar, M. Mushtaq, M.H.K. Rubel, R. Pandey, J. Madan, M.K.A. Mohammed, M.R. Islam, M.F. Rahman, Deep insights into the coupled optoelectronic and photovoltaic analysis of lead-free CsSnI3 perovskite-based solar cell using DFT calculations and SCAPS-1D simulations, ACS Omega (2023).
[13] Q. Ma, S. Huang, S. Chen, M. Zhang, C.F.J. Lau, M.N. Lockrey, H.K. Mulmudi, Y. Shan, J. Yao, J. Zheng, The effect of stoichiometry on the stability of inorganic cesium lead mixed-halide perovskites solar cells, J. Phys. Chem. C 121 (2017) 19642–19649.
[14] J.K. Nam, M.S. Jung, S.U. Chai, Y.J. Choi, D. Kim, J.H. Park, Unveiling the crystal formation of cesium lead mixed-halide perovskites for efficient and stable solar cells, J. Phys. Chem. Lett. 8 (2017) 2936–2940.
[15] M.E. Islam, M.R. Islam, S. Ahmmed, M.K. Hossain, M.F. Rahman, Highly efficient SnS-based inverted planar heterojunction solar cell with ZnO ETL, Phys. Scripta 98 (2023) 65501.
[16] J. Zhang, S. Wu, T. Liu, Z. Zhu, A.K. Jen, Boosting photovoltaic performance for lead halide perovskites solar cells with BF4− anion substitutions, Adv. Funct. Mater. 29 (2019) 1808833.
[17] Y. Zhou, L. You, S. Wang, Z. Ku, H. Fan, D. Schmidt, A. Rusydi, L. Chang, L. Wang, P. Ren, Giant photostriction in organic–inorganic lead halide perovskites, Nat. Commun. 7 (2016) 11193.
[18] T.R. Cook, D.K. Dogutan, S.Y. Reece, Y. Surendranath, T.S. Teets, D.G. Nocera, Solar energy supply and storage for the legacy and nonlegacy worlds, Chem. Rev. 110 (2010) 6474–6502.
[19] X. Huang, D. Ji, H. Fuchs, W. Hu, T. Li, Recent progress in organic phototransistors: semiconductor materials, device structures and optoelectronic applications, ChemPhotoChem 4 (2020) 9–38.
[20] M. Petrović, V. Chellappan, S. Ramakrishna, Perovskites: solar cells & engineering applications–materials and device developments, Sol. Energy 122 (2015) 678–699.
[21] T.W. Kelley, P.F. Baude, C. Gerlach, D.E. Ender, D. Muyres, M.A. Haase, D.E. Vogel, S.D. Theiss, Recent progress in organic electronics: materials, devices, and processes, Chem. Mater. 16 (2004) 4413–4422.
[22] W. Yin, T. Shi, Y. Yan, Unique properties of halide perovskites as possible origins of the superior solar cell performance, Adv. Mater. 26 (2014) 4653–4658.
[23] H. Wang, Z. Zeng, P. Xu, L. Li, G. Zeng, R. Xiao, Z. Tang, D. Huang, L. Tang, C. Lai, Recent progress in covalent organic framework thin films: fabrications, applications and perspectives, Chem. Soc. Rev. 48 (2019) 488–516.
[24] M.M. Abdelhamied, Y. Song, W. Liu, X. Li, H. Long, K. Wang, B. Wang, P. Lu, Improved photoemission and stability of 2D organic-inorganic lead iodide perovskite films by polymer passivation, Nanotechnology 31 (2020) 42LT01.
[25] J. Di, J. Chang, S. Liu, Recent progress of two-dimensional lead halide perovskite single crystals: crystal growth, physical properties, and device applications, EcoMat 2 (2020) e12036.
[26] Best Research-Cell Efficiencies, 2025, p. 2025.
[27] D.M. Hoat, T. V Vu, M.M. Obeid, H.R. Jappor, Assessing optoelectronic properties of PbI2 monolayer under uniaxial strain from first principles calculations, Superlattice. Microst. 130 (2019) 354–360.
[28] H.-J. Feng, Q. Zhang, Predicting efficiencies> 25% A3MX3 photovoltaic materials and Cu ion implantation modification, Appl. Phys. Lett. 118 (2021).
[29] M. Roknuzzaman, K. Ostrikov, H. Wang, A. Du, T. Tesfamichael, Towards lead-free perovskite photovoltaics and optoelectronics by ab-initio simulations, Sci. Rep. 7 (2017) 14025.
[30] F. Karsch, A. Patkos, P. Petreczky, Screened perturbation theory, Phys. Lett. B 401 (1997) 69–73.
[31] M.R. Islam, M.R.H. Mojumder, R. Moshwan, A.S.M.J. Islam, M.A. Islam, M. S. Rahman, M.H. Kabir, Strain-driven optical, electronic, and mechanical properties of inorganic halide perovskite CsGeBr3, ECS J. Solid State Sci. Technol. 11 (2022) 33001.
[32] J.P. Perdew, A. Zunger, Self-interaction correction to density-functional approximations for many-electron systems, Phys. Rev. B 23 (1981) 5048.
[33] D.-K. Seo, N. Gupta, M.-H. Whangbo, H. Hillebrecht, G. Thiele, Pressure-induced changes in the structure and band gap of CsGeX3 (X= Cl, Br) studied by electronic band structure calculations, Inorg. Chem. 37 (1998) 407–410.
[34] M.F. Rahman, M.A. Rahman, M.R. Islam, A. Ghosh, M.A. Bashar Shanto, M. Chowdhury, M. Al Ijajul Islam, M.H. Rahman, M.K. Hossain, M.A. Islam, Unraveling the strain-induced and spin-orbit coupling effect of novel inorganic halide perovskites of Ca3AsI3 using DFT, AIP Adv. 13 (2023) 1–15, https://doi.org/10.1063/5.0156961.
[35] U. Schwarz, F. Wagner, K. Syassen, H. Hillebrecht, Effect of pressure on the optical-absorption edges of CsGeBr 3 and CsGeCl 3, Phys. Rev. B 53 (1996) 12545.
[36] C.-C. Liu, W. Feng, Y. Yao, Quantum spin Hall effect in silicene and two-dimensional germanium, Phys. Rev. Lett. 107 (2011) 76802.
[37] D. Liu, Q. Li, H. Jing, K. Wu, Pressure-induced effects in the inorganic halide perovskite CsGeI 3, RSC Adv. 9 (2019) 3279–3284.
[38] M. Pandey, K.W. Jacobsen, K.S. Thygesen, Band gap tuning and defect tolerance of atomically thin two-dimensional organic–inorganic halide perovskites, J. Phys. Chem. Lett. 7 (2016) 4346–4352.

[39] M.R. Islam, M.S. Islam, N. Ferdous, K.N. Anindya, A. Hashimoto, Spin–orbit coupling effects on the electronic structure of two-dimensional silicon carbide, J. Comput. Electron. 18 (2019) 407–414, https://doi.org/10.1007/s10825-019-01326-2.
[40] R.J. Elliott, Theory of the effect of spin-orbit coupling on magnetic resonance in some semiconductors, Phys. Rev. 96 (1954) 266.
[41] P.C. Chow, L. Liu, Relativistic effects on the electronic band structure of compound semiconductors, Phys. Rev. 140 (1965) A1817.
[42] I.K.G.G. Apurba, M.R. Islam, M.S. Rahman, M.F. Rahman, J. Park, Tuning the physical properties of inorganic novel perovskite materials Ca3PX3 (X=I, Br and Cl): density function theory, Heliyon 10 (2024) e29144, https://doi.org/10.1016/j.heliyon.2024.e29144.
[43] I.K.G.G. Apurba, M.R. Islam, R. Khan, M.R.U. Nasib, M.F. Rahman, F.I. Bakhsh, A. Zahid, S. Ahmad, The density function theory analysis of the inorganic perovskite materials Mg3AsX3 (X=I, Br, Cl, and F): Alteration of the physical properties by strain effect, Mater. Sci. Semicond. Process. 183 (2024) 108741, https://doi.org/10.1016/j.mssp.2024.108741.
[44] M.F. Rahman, M.A. Rahman, M.R. Islam, A. Ghosh, M.A. Bashar Shanto, M. Chowdhury, M. Al Ijajul Islam, M.H. Rahman, M.K. Hossain, M.A. Islam, Unraveling the strain-induced and spin–orbit coupling effect of novel inorganic halide perovskites of Ca3AsI3 using DFT, AIP Adv. 13 (2023) 85329, https://doi.org/10.1063/5.0156961.
[45] M.F. Rahman, M.A.I. Islam, M.R. Islam, M.H. Ali, P. Barman, M.A. Rahman, M. Harun-Or-Rashid, M. Hasan, M.K. Hossain, Investigation of a novel inorganic cubic perovskite Ca 3 PI 3 with unique strain-driven optical, electronic, and mechanical properties, Nano Sel (2023) 1–14, https://doi.org/10.1002/nano.202300066.
[46] P. Giannozzi, S. Baroni, N. Bonini, M. Calandra, R. Car, C. Cavazzoni, D. Ceresoli, G.L. Chiarotti, M. Cococcioni, I. Dabo, Quantum espresso: a modular and open-source software project for quantum simulations of materials, J. Phys. Condens. Matter 21 (2009) 395502.
[47] J.P. Perdew, K. Burke, M. Ernzerhof, Generalized gradient approximation made simple, Phys. Rev. Lett. 77 (1996) 3865.
[48] R.L. Jones, R.K. Shideler, G.L. Cockerell, Association of Clostridium difficile with foal diarrhea, in: Proc. 5th Int. Conf. Equine Infect. Dis., University Press of Kentucky, 1988, pp. 236–240.
[49] P. Giannozzi, O. Andreussi, T. Brumme, O. Bunau, M.B. Nardelli, M. Calandra, R. Car, C. Cavazzoni, D. Ceresoli, M. Cococcioni, Advanced capabilities for materials modelling with Quantum ESPRESSO, J. Phys. Condens. Matter 29 (2017) 465901.
[50] J. Islam, A.K.M.A. Hossain, Semiconducting to metallic transition with outstanding optoelectronic properties of CsSnCl3 perovskite under pressure, Sci. Rep. 10 (2020) 14391.
[51] S. Bhattacharyya, A.K. Singh, Semiconductor-metal transition in semiconducting bilayer sheets of transition-metal dichalcogenides, Phys. Rev. B 86 (2012) 75454.
[52] A.P. Nayak, S. Bhattacharyya, J. Zhu, J. Liu, X. Wu, T. Pandey, C. Jin, A.K. Singh, D. Akinwande, J.-F. Lin, Pressure-induced semiconducting to metallic transition in multilayered molybdenum disulphide, Nat. Commun. 5 (2014) 3731.
[53] M.R. Islam, Z. Wang, S. Qu, K. Liu, Z. Wang, The impact of spin–orbit coupling and the strain effect on monolayer tin carbide, J. Comput. Electron. 20 (2021) 151–160.
[54] U.-G. Jong, C.-J. Yu, Y.-S. Kim, Y.-H. Kye, C.-H. Kim, First-principles study on the material properties of the inorganic perovskite Rb 1− x Cs x PbI 3 for solar cell applications, Phys. Rev. B 98 (2018) 125116.
[55] Z. Deng, Z. Zhu, I.-H. Chu, S.P. Ong, Data-driven first-principles methods for the study and design of alkali superionic conductors, Chem. Mater. 29 (2017) 281–288.
[56] N.J.J. De Klerk, I. Rosłoń, M. Wagemaker, Diffusion mechanism of Li argyrodite solid electrolytes for Li-ion batteries and prediction of optimized halogen doping: the effect of Li vacancies, halogens, and halogen disorder, Chem. Mater. 28 (2016) 7955–7963.
[57] A.R. Stamminger, B. Ziebarth, M. Mrovec, T. Hammerschmidt, R. Drautz, Ionic conductivity and its dependence on structural disorder in halogenated argyrodites Li6PS5X (X= Br, Cl, I), Chem. Mater. 31 (2019) 8673–8678.
[58] R.P. Rao, S. Adams, Studies of lithium argyrodite solid electrolytes for all-solid-state batteries, Phys. Status Solidi 208 (2011) 1804–1807.
[59] M.A. Kraft, S.P. Culver, M. Calderon, F. Böcher, T. Krauskopf, A. Senyshyn, C. Dietrich, A. Zevalkink, J. Janek, W.G. Zeier, Influence of lattice polarizability on the ionic conductivity in the lithium superionic argyrodites Li6PS5X (X= Cl, Br, I), J. Am. Chem. Soc. 139 (2017) 10909–10918.
[60] H. Deiseroth, S. Kong, H. Eckert, J. Vannahme, C. Reiner, T. Zaiß, M. Schlosser, Li6PS5X: a class of crystalline Li-rich solids with an unusually high Li+ mobility, Angew. Chem. 120 (2008) 767–770.
[61] C. Yu, S. Ganapathy, J. Hageman, L. Van Eijck, E.R.H. Van Eck, L. Zhang, T. Schwietert, S. Basak, E.M. Kelder, M. Wagemaker, Facile synthesis toward the optimal structure-conductivity characteristics of the argyrodite Li6PS5Cl solid-state electrolyte, ACS Appl. Mater. Interfaces 10 (2018) 33296–33306.
[62] C. Yu, F. Zhao, J. Luo, L. Zhang, X. Sun, Recent development of lithium argyrodite solid-state electrolytes for solid-state batteries: synthesis, structure, stability and dynamics, Nano Energy 83 (2021) 105858.
[63] P. Adeli, J.D. Bazak, A. Huq, G.R. Goward, L.F. Nazar, Influence of aliovalent cation substitution and mechanical compression on Li-ion conductivity and diffusivity in argyrodite solid electrolytes, Chem. Mater. 33 (2020) 146–157.
[64] P. Adeli, J.D. Bazak, K.H. Park, I. Kochetkov, A. Huq, G.R. Goward, L.F. Nazar, Boosting solid-state diffusivity and conductivity in lithium superionic argyrodites by halide substitution, Angew. Chem. Int. Ed. 58 (2019) 8681–8686.
[65] S. Boulineau, M. Courty, J.-M. Tarascon, V. Viallet, Mechanochemical synthesis of Li-argyrodite Li6PS5X (X= Cl, Br, I) as sulfur-based solid electrolytes for all solid state batteries application, Solid State Ionics 221 (2012) 1–5.
[66] L. Zhou, K.-H. Park, X. Sun, F. Lalère, T. Adermann, P. Hartmann, L.F. Nazar, Solvent-engineered design of argyrodite Li6PS5X (X= Cl, Br, I) solid electrolytes with high ionic conductivity, ACS Energy Lett. 4 (2018) 265–270.
[67] M.H.K. Rubel, M.A. Hossain, M.K. Hossain, K.M. Hossain, A.A. Khatun, M. M. Rahaman, M.F. Rahman, M.M. Hossain, J. Hossain, First-principles calculations to investigate structural, elastic, electronic, thermodynamic, and thermoelectric properties of CaPd3B4O12 (B= Ti, V) perovskites, Results Phys. 42 (2022) 105977.
[68] M.K. Hossain, G.F.I. Toki, A. Kuddus, M.H.K. Rubel, M.M. Hossain, H. Bencherif, M.F. Rahman, M.R. Islam, M. Mushtaq, An extensive study on multiple ETL and HTL layers to design and simulation of high-performance lead-free CsSnCl3-based perovskite solar cells, Sci. Rep. 13 (2023) 2521.
[69] H.-J. Feng, K. Wu, Z.-Y. Deng, Predicting inorganic photovoltaic materials with efficiencies> 26% via structure-relevant machine learning and density functional calculations, Cell Reports Phys. Sci. 1 (2020).
[70] S. Nair, M. Deshpande, V. Shah, S. Ghaisas, S. Jadkar, Cs2TlBiI6: a new lead-free halide double perovskite with direct band gap, J. Phys. Condens. Matter 31 (2019) 445902.
[71] B. Ehrler, E. Alarcón-Lladó, S.W. Tabernig, T. Veeken, E.C. Garnett, A. Polman, Photovoltaics Reaching for the Shockley–Queisser Limit, 2020.
[72] A.P. Nayak, T. Pandey, D. Voiry, J. Liu, S.T. Moran, A. Sharma, C. Tan, C.H. Chen, L.J. Li, M. Chhowalla, J.F. Lin, A.K. Singh, D. Akinwande, Pressure-dependent optical and vibrational properties of monolayer molybdenum disulfide, Nano Lett. 15 (2015) 346–353, https://doi.org/10.1021/nl5036397.
[73] Z. Xie, L. Hui, J. Wang, Z. Chen, C. Li, Electronic and optical properties of monolayer black phosphorus induced by bi-axial strain, Comput. Mater. Sci. 144 (2018) 304–314.
[74] M.A. Fadla, B. Bentria, T. Dahame, A. Benghia, First-principles investigation on the stability and material properties of all-inorganic cesium lead iodide perovskites CsPbI3 polymorphs, Phys. B Condens. Matter 585 (2020) 412118.
[75] R. Islam, K. Liu, Z. Wang, S. Hasan, Y. Wu, S. Qu, Z. Wang, Strain-induced electronic and optical properties of inorganic lead halide perovskites APbBr3 (A= Rb and Cs), Mater. Today Commun. 31 (2022) 103305, https://doi.org/10.1016/j.mtcomm.2022.103305.
[76] Z. Jellil, H. Ez-Zahraouy, Pressure-induced band gap engineering and enhanced optoelectronic properties of non-toxic Ca-based perovskite CsCaCl3: insights from density functional theory, Comput. Condens. Matter 38 (2024) e00879.
[77] M. Born, On the stability of crystal lattices. I, in: Math. Proc. Cambridge Philos. Soc., Cambridge University Press, 1940, pp. 160–172.
[78] Y. Benkrima, D. Belfennache, R. Yekhlef, A.M. Ghaleb, First-principle investigations of structural and optical properties of CdSe, Chalcogenide Lett. 20 (2023) 609–618, https://doi.org/10.15251/CL.2023.208.609.
[79] D. Allali, A. Bouhemadou, F. Zerarga, F. Sahnoune, Electronic and optical properties of the spinel oxides GeB2O4 (B= Mg, Zn and Cd): an ab-initio study, J. Nanoelectron. Optoelectron. 14 (2019) 945–952.
[80] M.R. Islam, B.K. Moghal, R. Moshwan, Tuning the electronic, optical, and thermal properties of cubic perovskites CsPbCl3-nBrn (n= 0, 1, 2, and 3) through altering the halide ratio, Phys. Scripta 97 (2022) 65704.
[81] S.F. Pugh, XCII. Relations between the elastic moduli and the plastic properties of polycrystalline pure metals, London, Edinburgh, Dublin Philos. Mag. J. Sci. 45 (1954) 823–843.
[82] M.H.K. Rubel, S.K. Mitro, K.M. Hossain, M.M. Rahaman, M.K. Hossain, J. Hossain, B.K. Mondal, I. Ahmed, A. Islam, A. El-Denglawey, A comprehensive first principles calculations on (Ba0. 82K0. 18)(Bi0. 53Pb0. 47) O3 single-cubic-perovskite superconductor, ArXiv Prepr. ArXiv2112 (2021) 03642.
[83] R. Majumder, S.K. Mitro, B. Bairagi, Influence of metalloid antimony on the physical properties of palladium-based half-Heusler compared to the metallic bismuth: a first-principle study, J. Alloys Compd. 836 (2020) 155395.
[84] M.A. Sarker, M.M. Hasan, M. Al Momin, A. Irfan, M.R. Islam, A. Sharif, Band gap engineering in lead free halide cubic perovskites GaGeX 3 (X = Cl, Br, and I) based on first-principles calculations, RSC Adv. 14 (2024) 9805–9818, https://doi.org/10.1039/d4ra00224e.
[85] D.H. Chung, W.R. Buessem, The elastic anisotropy of crystals, J. Appl. Phys. 38 (1967) 2010–2012.
[86] X. Gao, Y. Jiang, R. Zhou, J. Feng, Stability and elastic properties of Y–C binary compounds investigated by first principles calculations, J. Alloys Compd. 587 (2014) 819–826.
[87] P. Ravindran, L. Fast, P.A. Korzhavyi, B. Johansson, J. Wills, O. Eriksson, Density functional theory for calculation of elastic properties of orthorhombic crystals: application to TiSi 2, J. Appl. Phys. 84 (1998) 4891–4904.
[88] Z. Sun, S. Li, R. Ahuja, J.M. Schneider, Calculated elastic properties of M2AlC (M= Ti, V, Cr, Nb and Ta), Solid State Commun. 129 (2004) 589–592.
[89] X. Chang, W. Li, L. Zhu, H. Liu, H. Geng, S. Xiang, J. Liu, H. Chen, Carbon-based CsPbBr3 perovskite solar cells: all-ambient processes and high thermal stability, ACS Appl. Mater. Interfaces 8 (2016) 33649–33655.
[90] H.-J. Feng, Q. Zhang, Supplementary Material Predicting Efficiencies>25% A 3 MX 3 Photovoltaic Materials and Cu Ion Implantation Modification, (n.d.).
[91] C.M. Fang, K. V Ramanujachary, H.T. Hintzen, G. De With, E Lectronic Structure of Magnesium Nitride-Fluorides from First-Principles Calculations, vol. 351, 2003, pp. 72–76.